Forest Chemicals Review
www.forestchemicalsreview.com
ISSN: 1520-0191
September-October 2022 Page No. 672-682
Article History: Received: 06 April 2022, Revised: 28 April 2022, Accepted: 04 May 2022, Publication: 15 May 2022

Anti-Integral Saturation-based Control Technology in PMSM High Frequency Injection

Jianduo Dou, Jianning Lu*
School of Electrical and Electronic Engineering, Shanghai Institute of Technology, Shanghai, China
*Corresponding Author.

Abstract:

In sensorless low-speed control of built-in permanent magnet synchronous motor (IPMSM) based on the traditional high-frequency injection method, the current regulation process has integral saturation, leading to slow desaturation and overcharge acceleration. In order to solve this problem, the mechanism of its occurrence is analyzed and studied in detail. An anti-saturation control algorithm is proposed herein to integrate the control input saturation error and add it to the integral term of PI through an adaptive system. The simulation experiment results show that the method can effectively reduce the overshoot of the speed control system, shorten the system stability time, and at the same time increase the system robustness to the load disturbance.

Keywords*: Permanent magnet synchronous motor, Pulsed high-frequency voltage injection, Sensorless vector control, Anti-integral saturation PID control.*

I. INTRODUCTION

Divided by the speed area, sensorless control technology of permanent magnet synchronous motor (PMSM) consists of medium and high speed control and low speed control technology [1]. Medium and high speed control usually adopts the method based on the fundamental wave model of the motor, which is mainly to detect the back electromotive force and then use the motor model to estimate the rotor position information, including sliding mode observer, extended Kalman filter, model reference adaptive model contro [2, [3]. However, in the case of low speed or even zero speed, the back EMF has too small amplitude and too low signal-to-noise ratio to support accurate extraction for the rotor position estimation [4]. By contrast, the high-frequency injection method demonstrates great advantages at low speed and zero speed [5, [6]. The high-frequency injection method is based on the electrode saliency. Since the inductance matrix of the PMSM high-frequency model contains the rotor position information, the rotor position can be extracted from the response signal by injecting high-frequency voltage or current signals[7].

This paper firstly analyzes the mathematical model of IPMSM, and then studies the anti-integral saturation IPMSM sensorless vector control system based on pulsed high frequency injection method[8]. In view of the inherent integral saturation problem in control, the mechanism of its occurrence is analyzed and studied in detail. The control input saturation error is integrated and added to the integral term in the PI

Forest Chemicals Review
www.forestchemicalsreview.com
ISSN: 1520-0191
September-October 2022 Page No. 672-682
Article History: Received: 06 April 2022, Revised: 28 April 2022, Accepted: 04 May 2022, Publication: 15 May 2022

control through adaptive coefficient adjustment[9]. The simulation results show that the control strategy proposed herein has good dynamic response and steady-state response, achieves accurate position and speed estimation, and the system has strong robustness[10].

II. IPMSM MATHEMATICAL MODEL

The voltage mathematical model of the IPMSM in the two-phase synchronous rotating d - q coordinate system is as follows:

$$\begin{bmatrix} u_d \\ u_q \end{bmatrix} = R_s \begin{bmatrix} i_d \\ i_q \end{bmatrix} + \begin{bmatrix} L_d & 0 \\ 0 & L_q \end{bmatrix} p \begin{bmatrix} i_d \\ i_q \end{bmatrix} + \omega_e \begin{bmatrix} 0 & -L_q \\ L_d & 0 \end{bmatrix} \begin{bmatrix} i_d \\ i_q \end{bmatrix} + \omega_e \begin{bmatrix} 0 \\ \psi_f \end{bmatrix} \tag{1}$$

Where, R_s is the stator winding resistance, u_d , u_q are the corresponding two-phase voltages on the axes d , q . i_d , i_d are the two-phase currents corresponding to the axes d , q . L_d , L_q are the direct-axis inductance and the quadrature-axis inductance, respectively, ω_e is the rotor electrical angular velocity, and ψ_f is the permanent magnet flux linkage.

The transformation matrix from the d - q coordinate system to the two-phase stationary α - β coordinate system is as follows:

$$T = \begin{bmatrix} \cos\theta_r & -\sin\theta_r \\ \sin\theta_r & \cos\theta_r \end{bmatrix} \tag{2}$$

By transforming equation (1) into a two-phase stationary-coordinate α - β system through a transformation matrix, there is:

$$\begin{bmatrix} u_\alpha \\ u_\beta \end{bmatrix} = \begin{bmatrix} L_0 + L_1\cos(2\theta_r) & L_1\sin(2\theta_r) \\ L_1\sin(2\theta_r) & L_0 - L_1\cos(2\theta_r) \end{bmatrix} p \begin{bmatrix} i_\alpha \\ i_\beta \end{bmatrix} + R_S \begin{bmatrix} i_\alpha \\ i_\beta \end{bmatrix}$$
$$+\omega_e\psi_f \begin{bmatrix} -\sin\theta_r \\ \cos\theta_r \end{bmatrix} + 2\omega_e \begin{bmatrix} -\sin(2\theta_r) & \cos(2\theta_r) \\ \cos(2\theta_r) & \sin(2\theta_r) \end{bmatrix} \begin{bmatrix} i_\alpha \\ i_\beta \end{bmatrix} \tag{3}$$

Where, u_α , u_β are the α - β axis voltage components; i_α , i_β are the α , β axis current components, respectively; L_0 is the average inductance, $L_0 = \left(L_d + L_q\right)/2$; θ_r is the actual rotor electrical angle; L_1 is the differential inductance, $L_1 = \left(L_d - L_q\right)/2$.

When injecting a high-frequency voltage signal into the stator group, if the signal frequency is much higher than the fundamental frequency, the motor can be regarded as a pure inductive load, and the related

Forest Chemicals Review
www.forestchemicalsreview.com
ISSN: 1520-0191
September-October 2022 Page No. 672-682
Article History: Received: 06 April 2022, Revised: 28 April 2022, Accepted: 04 May 2022, Publication: 15 May 2022

two values of equation (3) and ω_e are very small under low speed, which can be ignored, so the high excitation voltage equation under the two stationary coordinates is:

$$\begin{bmatrix} u_{\alpha h} \\ u_{\beta h} \end{bmatrix} = \begin{bmatrix} L_0 + L_1\cos(2\theta_r) & L_1\sin(2\theta_r) \\ L_1\sin(2\theta_r) & L_0 - L_1\cos(2\theta_r) \end{bmatrix} p \begin{bmatrix} i_{\alpha h} \\ i_{\beta h} \end{bmatrix} \tag{4}$$

Where, $u_{\alpha h}$, $u_{\beta h}$ are the high-frequency voltage components of axes α , β , respectively; $i_{\alpha h}$, $i_{\beta h}$ are the high-frequency current components of the axes α , β respectively.

By transforming formula (4), there is:

$$p\begin{bmatrix} i_{\alpha h} \\ i_{\beta h} \end{bmatrix} = \frac{1}{L_0^2 - L_1^2}\begin{bmatrix} L_0 - L_1\cos(2\theta_r) & -L_1\sin(2\theta_r) \\ -L_1\sin(2\theta_r) & L_0 + L_1\cos(2\theta_r) \end{bmatrix}\begin{bmatrix} u_{\alpha h} \\ u_{\beta h} \end{bmatrix} \tag{5}$$

III. PULSED HIGH-FREQUENCY VOLTAGE INJECTION CONTROL STRATEGY BASED ON ANTI-INTEGRAL SATURATION

3.1 Pulsed High Frequency Injection

In Figure 1, α - β is a two-phase stationary coordinate system, $\hat{\theta}_r$ is the estimated rotor position angle, and θ_r is the actual rotor position angle. The angle $\tilde{\theta}_r$ between the estimated rotor synchronous rotating coordinate system $\hat{d}$ - $\hat{q}$ and the actual rotor synchronous rotating coordinate system d - q is the estimated error angle for the rotor:

$$\tilde{\theta}_r = \theta_r - \hat{\theta}_r \tag{6}$$

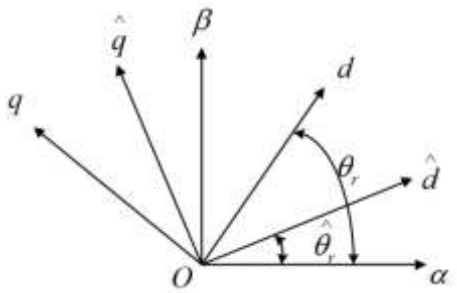

Fig 1 The relationship between the estimated rotor and the actual rotor synchronous rotating coordinate system

Forest Chemicals Review
www.forestchemicalsreview.com
ISSN: 1520-0191
September-October 2022 Page No. 672-682
Article History: Received: 06 April 2022, Revised: 28 April 2022, Accepted: 04 May 2022, Publication: 15 May 2022

The voltage equation of the motor in the synchronous rotating coordinate system d - q is:

$$\begin{cases} u_{din}^{r} \approx L_d \dfrac{di_{din}^{r}}{dt} \\ u_{qin}^{r} \approx L_q \dfrac{di_{qin}^{r}}{dt} \end{cases} \tag{7}$$

In the synchronous rotating coordinate system d - q , the motor stator inductance is:

$$L_{dq} = \begin{bmatrix} L_d & 0 \\ 0 & L_q \end{bmatrix} \tag{8}$$

In the stationary coordinate system α - β , equation (7) is transformed into:

$$L_{\alpha\beta} = \begin{bmatrix} L + \Delta L \cos 2\theta_r & -\Delta L \sin 2\theta_r \\ -\Delta L \sin 2\theta_r & L - \Delta L \cos 2\theta_r \end{bmatrix} \tag{9}$$

Then, in the estimated rotor synchronous rotating coordinate system $\hat{d}$ - $\hat{q}$, the relationship between high-frequency voltage and current is expressed as:

$$\begin{bmatrix} \frac{d\hat{i}_{din}^{r}}{dt} \\ \frac{d\hat{i}_{qin}^{r}}{dt} \end{bmatrix} = \begin{bmatrix} \cos\tilde{\theta}_r & -\sin\tilde{\theta}_r \\ \sin\tilde{\theta}_r & \cos\tilde{\theta}_r \end{bmatrix} \times \begin{bmatrix} \frac{1}{L_d} & 0 \\ 0 & \frac{1}{L_q} \end{bmatrix} \times \begin{bmatrix} \cos\tilde{\theta}_r & \sin\tilde{\theta}_r \\ -\sin\tilde{\theta}_r & \cos\tilde{\theta}_r \end{bmatrix} \begin{bmatrix} \hat{u}_{din}^{r} \\ \hat{u}_{qin}^{r} \end{bmatrix} \tag{10}$$

Where, $\hat{u}_{din}^{r}$, $\hat{u}_{qin}^{r}$ and $\hat{i}_{din}^{r}$, $\hat{i}_{qin}^{r}$ are the high-frequency components of the voltage and current in axes $\hat{d}$, $\hat{q}$ of the estimated rotor synchronous rotating coordinate system $\hat{d}$ - $\hat{q}$, respectively. If the average inductance and the difference inductance are used, Equation (10) is obtained

$$\begin{cases} \frac{d\hat{i}_{din}^{r}}{dt} = \frac{1}{L^2 - \Delta L^2}\left[(L + \Delta L \cos 2\tilde{\theta}_r)\hat{u}_{din}^{r} + \Delta L \sin 2\tilde{\theta}_r \hat{u}_{qin}^{r} \right] \\ \frac{d\hat{i}_{qin}^{r}}{dt} = \frac{1}{L^2 - \Delta L^2}\left[\Delta L \sin 2\tilde{\theta}_r \hat{u}_{din}^{r} + (L - \Delta L \cos 2\tilde{\theta}_r)\hat{u}_{qin}^{r} \right] \end{cases} \tag{11}$$

This method only injects high frequency voltage to the axis d ,

Forest Chemicals Review
www.forestchemicalsreview.com
ISSN: 1520-0191
September-October 2022 Page No. 672-682
Article History: Received: 06 April 2022, Revised: 28 April 2022, Accepted: 04 May 2022, Publication: 15 May 2022

$$\begin{cases} \hat{u}_{din}^{r} = u_{in}\cos\omega_{in}t \\ \hat{u}_{qin}^{r} = 0 \end{cases} \tag{12}$$

Where, u_{in} is the amplitude of the high-frequency voltage signal, and ω_{in} is the frequency of the high-frequency voltage signal.

At this time, the high frequency current is:

$$\begin{cases} \hat{i}_{dsi}^{r} = \dfrac{V_i \sin\omega_i t}{\omega_i\left(L^2-\Delta L^2\right)}\left(L+\Delta L\cos 2\tilde{\theta}_r\right) \\ \hat{i}_{qsi}^{r} = \dfrac{V_i \sin\omega_i t}{\omega_i\left(L^2-\Delta L^2\right)}\left(\Delta L\sin 2\tilde{\theta}_r\right) \end{cases} \tag{13}$$

3.2 Traditional Current-Regulated PI Controller

The current loop is to enhance the system rapidity, suppress the internal interference of the current loop, etc. Compared with the speed loop, the current inner loop generally only relates to the PWM inverter and motor parameters, which is not affected by external load changes. Axis d is designed in the same way as axis q. Now, we take axis d as an example.

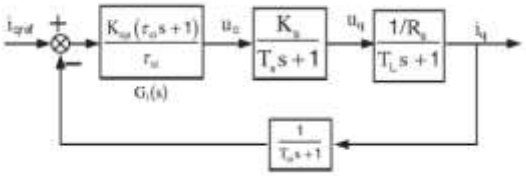

Fig 2 Current loop controller

The open-loop transfer function of the current loop is:

$$G_i(s) = \frac{K_{cp}K_s\left(\tau_{ci}s+1\right)/R_s}{\tau_{ci}s\left(T_{oi}s+1\right)\left(T_L s+1\right)\left(T_s s+1\right)} \tag{14}$$

The rotor position estimator as shown in Figure 2 includes a PI regulator and an integrator, and the transfer function from the actual rotor position to the estimated value can be expressed as:

Forest Chemicals Review
www.forestchemicalsreview.com
ISSN: 1520-0191
September-October 2022 Page No. 672-682
Article History: Received: 06 April 2022, Revised: 28 April 2022, Accepted: 04 May 2022, Publication: 15 May 2022

$$\frac{\theta_r}{\theta_r} = \frac{K_p K_{err} s + K_i K_{err}}{s^2 + K_p K_{err} s + K_i K_{err}} \tag{15}$$

Where, K_p and K_i are the proportional and integral coefficients of the PI regulator, respectively.

The transfer function in equation (11) has a gain of 1 under steady state, which means the estimator can achieve unbiased estimate of the rotor position, so the low-pass filter used to eliminate fluctuations in the estimated speed value can be omitted.

3.3 Anti-Integral Saturation-Based Current Regulation PI Controller

The anti-integral saturation control idea described in Figure 3 is as follows: Integrate the control input saturation error $u_n - u_s$ and add it to the integral term in PI control through adaptive coefficient adjustment.

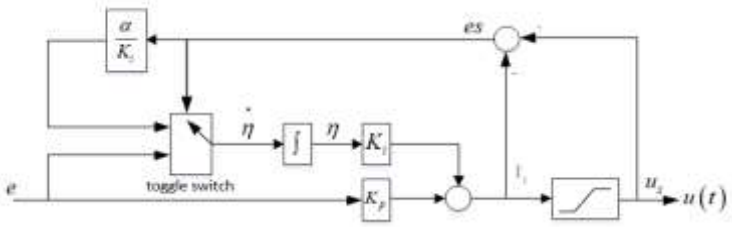

Fig 3 PI controller structure based on anti-saturation

The PI control algorithm for anti-saturation variable structure is as follows: the coefficient η is used to achieve self-adaptive adjustment of the integral term, and the self-adaptive change law is as follows:

$$\eta = \begin{cases} -\alpha\left(u_n - u_s\right)/k_i, & u_n \neq u_s, e\left(u_n - \bar{u}\right) > 0 \\ e & u_n = u_s \end{cases} \tag{16}$$

Where, $\bar{u} = \left(u_{\min} + u_{\max}\right)/2; \alpha > 0;$ $u_{\min}$ and $u_{\max}$ are the maximum and minimum values of the control input signal.

IV. SIMULATION AND ANALYSIS OF EXPERIMENTAL RESULTS

4.1 Simulation

MATLAB/Simulink is used to establish each functional sub-module, and then each sub-module is formed into a system simulation model. IPMSM sensorless control is injected into the pulsed high

Forest Chemicals Review
www.forestchemicalsreview.com
ISSN: 1520-0191
September-October 2022 Page No. 672-682
Article History: Received: 06 April 2022, Revised: 28 April 2022, Accepted: 04 May 2022, Publication: 15 May 2022

frequency voltage of the traditional PI controller and IPMSM sensorless control is injected into the pulsed high frequency based on anti-integral saturation respectively for verification. The Figure 4 is the IPMSM sensorless control block diagram.

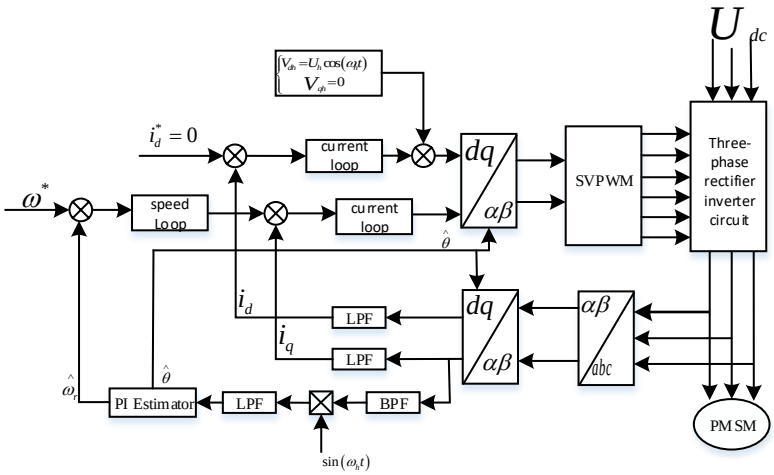

Fig 4. IPMSM sensorless control block diagram

The parameters for the motor in the simulation model and actual motor are as follows: rated voltage 380V; rated current 2.7A; rated power 1.5KW; rated speed 3000r/min; rated torque 4.7N·m; d axis inductance 17.97Mh; q axis inductance 57.42mH; number of pole pairs 2; stator resistance 2.2; magnetic flux 14Wb. The switching frequency in the simulation is 10kHz, and high-frequency sinusoidal voltage signal is injected into the d axis. The injection signal frequency is 1/8 of the switching frequency, that is, 1.25kHz. The injection signal has an amplitude of 50V, and the given motor speed is $100\,r\cdot\min^{-1}$. The speed curve of traditional PI controller and anti-integral saturation pulsed high-frequency voltage injection is Figure 5.

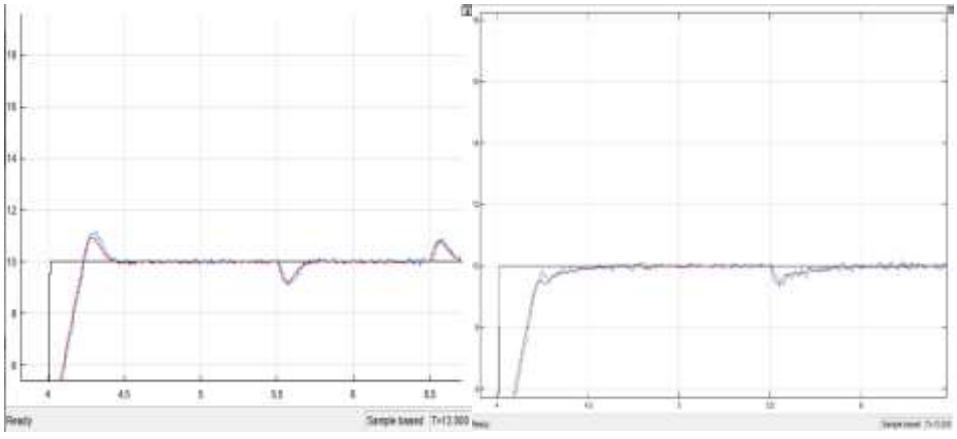

(a) Speed curve of traditional PI controller(b) Speed curve of anti-integral saturation PI controller

Fig 5 Comparison between speed curves of two PI controllers

Forest Chemicals Review
www.forestchemicalsreview.com
ISSN: 1520-0191
September-October 2022 Page No. 672-682
Article History: Received: 06 April 2022, Revised: 28 April 2022, Accepted: 04 May 2022, Publication: 15 May 2022

The speed simulation curves of the two PI controllers indicate that the IPMSM sensorless control strategy based on anti-integral saturation has good dynamic response and steady-state response, and accurate estimated position and estimated speed are achieved.

4.1 Experiment

The proposed anti-integral saturation sensorless control strategy is verified on the experimental platform. The IPMSM parameters in the experimental platform are the same as the simulation parameters. The experiment was performed on a 1.5KW IPMSM. The load torque was provided by a 25 $N \cdot m / 2A$ magnetic powder brake, and the load torque was adjusted by modulating the tension controller. The control algorithm was implemented by TMS320F28335 DSP, the actual rotor position was determined by the incremental encoder PENON-K3808G and compared with the estimated position.

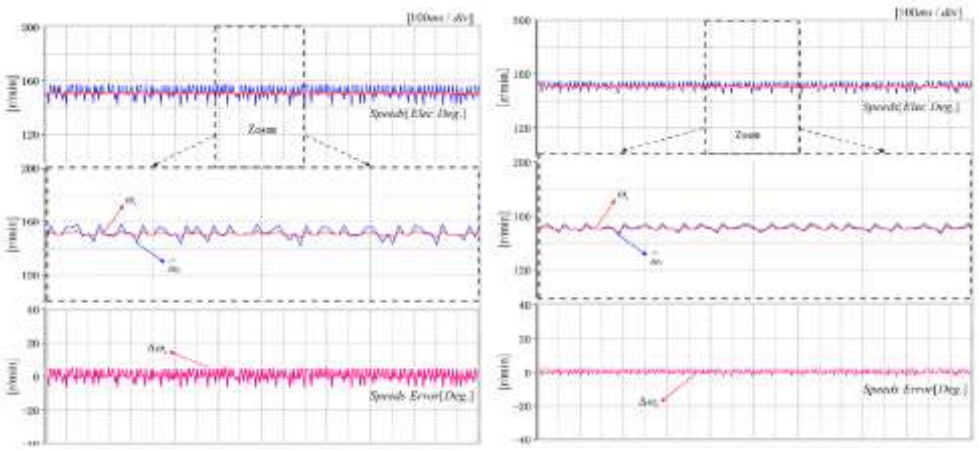

(a) Before optimization (b) After optimization

Fig 6 Speed experiment

(a) and (b) in Figure 6 display the experimental waveforms of the speed before and after the optimization of the PI controller, respectively. The blue curve in Figure 6 indicates estimated speed, the red curve indicates the actual speed. From top to bottom, there are actual speed, estimated speed, partial enlarged drawing of the speed, and the speed error. It can be observed in the experimental graph that the error between the estimated speed and the actual speed is significantly smaller after optimization. By further careful study of the partially enlarged waveform of the speed, we can clearly see the reduction in the error and the waveform approximation rule. Finally, the optimization scheme feasibility is determined by observing the waveform of the speed error. The validity of the research on the improvement of the position estimation error signal is also proved. The error of the rotor speed before the improvement fluctuates within the range of $6\,r/\min$, and the speed error range after the improvement is reduced to 1.8 $r/\min$. Through analysis of the above experimental results, it can be proved that the optimized scheme can better estimate the rotational speed accuracy.

Forest Chemicals Review
www.forestchemicalsreview.com
ISSN: 1520-0191
September-October 2022 Page No. 672-682
Article History: Received: 06 April 2022, Revised: 28 April 2022, Accepted: 04 May 2022, Publication: 15 May 2022

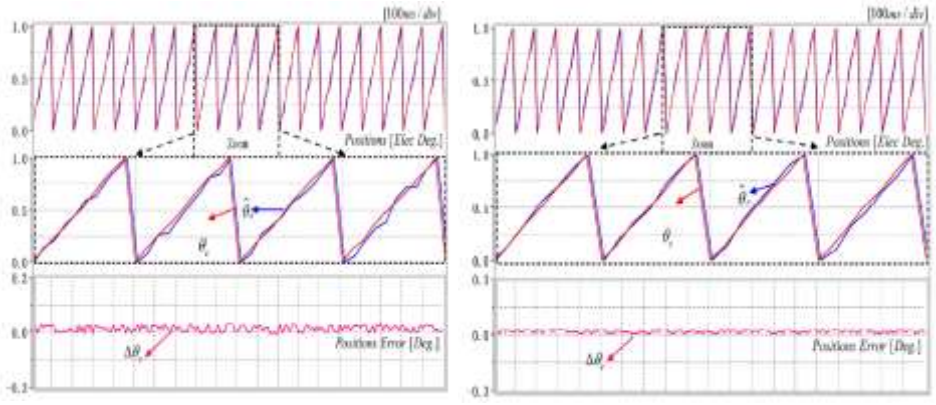

(a) Before optimization (b) After optimization

Fig 7 Rotor position experiment

Figure 7 is the experimental waveform of the rotor position, and the abscissa in the figure adopts the per unit value. Figures (a) and (b) are the experimental waveforms of the rotor position before and after the PI controller optimization, respectively. From top to bottom, there are actual rotor position, estimated rotor position, partial enlarged drawing of the position waveform and experimental diagram of the position error. According to the experimental diagram, after analyzing the experimental results of the rotor operating position and estimated position, it is concluded that after optimization, the estimated rotor position and the actual rotor position have better consistency. By carefully study of the partial enlarged waveform of the rotor position, we can clearly see that the improved rotor estimated position waveform converges more to the actual rotor position waveform after the optimization. By observing the rotor position error diagram, great position error can also be seen before optimization, with a maximum error of about $0.095\pi rad$, while the maximum position error after optimization is only about $0.07\pi rad$, so the position error has been reduced by 26% approximately.

In conclusion, the experimental results demonstrate practical engineering value of the sensorless control scheme based on anti-integral saturation. This scheme can make the estimated speed closer to the actual speed and result in higher estimated rotor position accuracy, which indicates that the sensorless control system has greater accuracy, which helps achieve the purpose of good motor control.

In order to further illustrate that the anti-integral saturation sensorless control scheme is applicable to the low-speed sensorless control operation, the pulsed high-frequency voltage injection method based on anti-integral saturation scheme was tested at different speeds, as shown in Figure 8.

Forest Chemicals Review
www.forestchemicalsreview.com
ISSN: 1520-0191
September-October 2022 Page No. 672-682
Article History: Received: 06 April 2022, Revised: 28 April 2022, Accepted: 04 May 2022, Publication: 15 May 2022

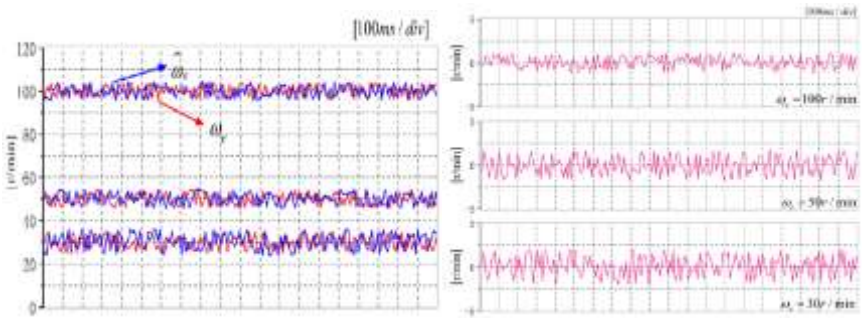

(a) Speed (b) Speed error

Fig 8 Experiments at different speeds

When the rotor speed is set to $30\,r/min$, $50\,r/min$, $100\,r/min$, the observed waveforms of the estimated speed and the actual speed are shown in Figure 8(a). The observed waveform of the rotor speed error when the rotor speed is set to $30\,r/min$, $50\,r/min$, and $100\,r/min$ is shown in Figure 8(b). By analysis of Figure (a), it can be concluded that the estimated speed curve fits the actual speed curve in the control of different speeds in the low-speed section of the motor, showing a good control effect. By analysis of the rotor error diagram in Figure (b), we can clearly see that the speed error does not fluctuate much under the three speeds, which further proves that the anti-integral saturation sensorless control scheme can optimize theoretical and practical application of sensorless control technology for pulsed high frequency electric injection method.

V. CONCLUSION

This paper studies sensorless control strategy for IPMSM based on high frequency injection method. In view of the integral saturation problem of PI controller, an anti-integral saturation control algorithm is proposed here, which integrates the control input saturation error and adds it to the PI integral term through an adaptive system. It effectively prevents integral saturation phenomenon, greatly lowers the overshoot during the acceleration process, thus greatly reducing steady-state error and accelerating the response. The experimental results prove that the method can effectively reduce the overshoot time and speed up the system response time. Moreover, the rotor position information and speed estimation effect is better, and the system also has strong robustness.

REFERENCES

[1] Li Yuanjiang, Dong Xin, Wei Haifeng, Zhang Yi, Li Keli. (2020) Composite PI sensorless control of speed loop in built-in permanent magnet synchronous motor Transactions of China Electrotechnical Society 35(10):2119-2129.
[2] Zhao Y, Qiao W, Wu L (2014). Improved Rotor Position and Speed Estimators for Sensorless Control of Interior Permanent-Magnet Synchronous. IEEE Journal of Emerging & Selected Topics in Power Electronics 2:627-639.
[3] Zhu Jun, Han Lili, Wang Xudong. (2013) Status and development trend of sensorless control of permanent

Forest Chemicals Review
www.forestchemicalsreview.com
ISSN: 1520-0191
September-October 2022 Page No. 672-682
Article History: Received: 06 April 2022, Revised: 28 April 2022, Accepted: 04 May 2022, Publication: 15 May 2022

magnet synchronous motor Micromotors 46: 11-16.

[4] Ni R, Xu DG, Blaabjerg F, et al. (2016) Square-Wave Voltage Injection Algorithm for PMSM Position Sensorless Control With High Robustness to Voltage Errors. IEEE Transactions on Power Electronics 1-1.

[5] Yi Jingshu. (2019) Research progress and key technologies of dual-motor drive synchronous control system. Applied EnergyTechnology 01:32-34.

[6] Liu Jinkun. (2011) MATLAB simulation of advanced PID control. Electronic Industry Press.

[7] Song Tongyue, Yan Jianhu, Ying Zhanfeng, Chi Song, Zhou Yi. (2020) Sensorless control of zero-low-speed permanent magnet linear synchronous motor based on pulsed high-frequency injection method. Motor and Control Application. 47: 10-17+24.

[8] Zhang H, Liu W, Chen Z, et al. (2020) Asymmetric Space Vector Modulation for PMSM Sensorless Drives Based on Square-Wave Voltage-Injection Method. IEEE Transactions on Industry Applications.1-1.

[9] Lin C, Sun J. (2019) An Improved Rotor Position Estimation Method for PMSM Based on Pulsating Square-Wave-Type Voltage Injection. IOP Conference Series: Materials ence and Engineering. 563:052101-.

[10] Fan Shengwen, Li Lei, Zheng Chunyu. (2017) Comparison and analysis of sensorless control with two high frequency signal injection methods. Control Engineering of China. 24(10): 2093-2098.